The WiggleZ Dark Energy Survey: constraining galaxy bias and cosmic growth with three-point correlation functions

Felipe A. Marín,[1]⋆ Chris Blake,[1] Gregory B. Poole,[1,2] Cameron K. McBride,[3]
Sarah Brough,[4] Matthew Colless,[4] Carlos Contreras,[1] Warrick Couch,[1]
Darren J. Croton,[1] Scott Croom,[5] Tamara Davis,[6] Michael J. Drinkwater,[6]
Karl Forster,[7] David Gilbank,[8] Mike Gladders,[9] Karl Glazebrook,[1] Ben Jelliffe,[5]
Russell J. Jurek,[10] I-hui Li,[11] Barry Madore,[12] D. Christopher Martin,[7]
Kevin Pimbblet,[13] Michael Pracy,[1,5] Rob Sharp,[14] Emily Wisnioski,[1,15]
David Woods,[16] Ted K. Wyder[7] and H. K. C. Yee[11]

[1]*Centre for Astrophysics & Supercomputing, Swinburne University of Technology, PO Box 218, Hawthorn, VIC 3122, Australia*
[2]*School of Physics, University of Melbourne, Parksville, VIC 3010, Australia*
[3]*Harvard–Smithsonian Center for Astrophysics, 60 Garden Street, Cambridge, MA 02138, USA*
[4]*Australian Astronomical Observatory, PO Box 915, North Ryde, NSW 1670, Australia*
[5]*Sydney Institute for Astronomy, School of Physics, University of Sydney, NSW 2006, Australia*
[6]*School of Mathematics and Physics, University of Queensland, Brisbane, QLD 4072, Australia*
[7]*California Institute of Technology, MC 278-17, 1200 East California Boulevard, Pasadena, CA 91125, USA*
[8]*South African Astronomical Observatory, PO Box 9 Observatory, 7935 South Africa*
[9]*Department of Astronomy and Astrophysics, University of Chicago, 5640 South Ellis Avenue, Chicago, IL 60637, USA*
[10]*Australia Telescope National Facility, CSIRO, Epping, NSW 1710, Australia*
[11]*Department of Astronomy and Astrophysics, University of Toronto, 50 St George Street, Toronto, ON M5S 3H4, Canada*
[12]*Observatories of the Carnegie Institute of Washington, 813 Santa Barbara St, Pasadena, CA 91101, USA*
[13]*School of Physics, Monash University, Clayton, VIC 3800, Australia*
[14]*Research School of Astronomy & Astrophysics, Australian National University, Weston Creek, ACT 2611, Australia*
[15]*Max Planck Institut für extraterrestrische Physik, Giessenbachstraβe, D-85748 Garching, Germany*
[16]*Department of Physics & Astronomy, University of British Columbia, 6224 Agricultural Road, Vancouver, BC V6T 1Z1, Canada*

ABSTRACT

Higher order statistics are a useful and complementary tool for measuring the clustering of galaxies, containing information on the non-Gaussian evolution and morphology of large-scale structure in the Universe. In this work we present measurements of the three-point correlation function (3PCF) for 187 000 galaxies in the WiggleZ spectroscopic galaxy survey. We explore the WiggleZ 3PCF scale and shape dependence at three different epochs $z = 0.35$, 0.55 and 0.68, the highest redshifts where these measurements have been made to date. Using N-body simulations to predict the clustering of dark matter, we constrain the linear and non-linear bias parameters of WiggleZ galaxies with respect to dark matter, and marginalize over them to obtain constraints on $\sigma_8(z)$, the variance of perturbations on a scale of 8 h^{-1} Mpc and its evolution with redshift. These measurements of $\sigma_8(z)$, which have 10–20 per cent accuracies, are consistent with the predictions of the Λ cold dark matter concordance cosmology and test this model in a new way.

Key words: methods: statistical – cosmological parameters – cosmology: observations – large-scale structure of – Universe.

1 INTRODUCTION

In the current structure formation paradigm (e.g. Press & Schechter 1974; White & Rees 1978; White & Frenk 1991; Berlind & Weinberg 2002), galaxies form inside dark matter (DM) haloes, which evolved from small perturbations in the early Universe. This

⋆E-mail: fmarin@astro.swin.edu.au

allows us to connect the galaxy field to the overall matter distribution, and therefore to use large-scale galaxy clustering to constrain cosmological models and their parameters (see for instance Peacock et al. 2001; Eisenstein et al. 2005; Percival et al. 2007; Kazin et al. 2010; Sánchez et al. 2012 and references therein). This connection, however, is not a perfect one, since galaxy observables such as luminosity, colour, etc. are also shaped by baryonic physics and environmental effects, with the consequence that different types of galaxies have different clustering properties (Norberg et al. 2001; Zehavi et al. 2005, 2011), described as 'galaxy bias'.

The galaxy two-point correlation functions (2PCF) have been the main tool to constrain cosmology using large-scale structure, because the shape of the two-point clustering of matter depends on cosmological parameters such as the matter density, baryon fraction and neutrino mass. In some cases, it is possible to obtain these constraints marginalizing over the bias of the galaxy populations we use; an example is the cosmological constraints from baryon acoustic oscillation (BAO) measurements (Cole et al. 2005; Eisenstein et al. 2005; Beutler et al. 2011; Blake et al. 2011a; Sánchez et al. 2012) where parameters such as the cosmic distance scale and the Hubble expansion rate $H(z)$ can be measured using only the position of the BAO peak, which does not depend on the details of the galaxy population used, at first order. However, there are other cosmological parameters which cannot be constrained using two-point galaxy clustering statistics only.

In particular, the amplitude of primordial perturbations, parametrized in the low-redshift Universe by $\sigma_8(z)$, the rms of the matter density field in 8 h^{-1} Mpc spheres extrapolated to redshift z by linear theory, is degenerate with the details of the galaxy population, encoded in the large-scale linear galaxy bias parameter b_1. On large scales, these two parameters have the same effect on the overall amplitude of the galaxy 2PCF; therefore, one can only constrain the product $b_1\sigma_8$.

Resolving this degeneracy requires use of another observable, or adoption of a particular galaxy evolution model. For the first approach, other observables such as lensing (e.g. Fu et al. 2008; Lin et al. 2012) or the mass function of galaxy clusters (e.g. Eke, Cole & Frenk 1996; Rozo et al. 2010; Kilbinger et al. 2013) have been used to constrain σ_8, but current constraints are degenerate with other parameters such as the matter density Ω_m. The second approach, selecting a particular galaxy population with a known evolution of its clustering, allows disentangling of the linear galaxy bias and σ_8, and has been studied in Tojeiro et al. (2012) using a passively evolving luminous subsample of Sloan Digital Sky Survey (SDSS)-I/II and SDSS-III galaxies. This method gives good constraints on σ_8, but whereas it works well for their galaxy sample (of luminous red galaxies, LRGs), for other galaxy surveys it might be difficult to find a suitable passive galaxy population.

Another, complementary way to break these degeneracies is to measure three-point correlation functions (3PCF) of the same galaxy data set. Two-point statistics are only a complete description for Gaussian fields, but the late-time large-scale structure, driven by non-linear gravitational clustering, is strongly non-Gaussian (Bernardeau et al. 2002), and higher order correlation functions thus encode additional information that can be used to constrain galaxy population and cosmological models. The first measurements of the 3PCF were carried out in angular catalogues as a way to verify the hierarchical model of structure formation (Peebles & Groth 1975), and more recently, in large-scale spectroscopic surveys such as 2dFGRS (Verde et al. 2002; Jing & Börner 2004; Gaztañaga et al. 2005) and SDSS (Kayo et al. 2004; Nichol et al. 2006; Kulkarni et al. 2007; Gaztanaga et al. 2008; Marín 2011; McBride et al. 2011b;

Guo et al. 2013). The main goal of these measurements is to test theories of growth of structure and the predictions of cosmological simulations, and to measure the biasing of the galaxies with respect to the DM distribution.

In this work, we present the results of the measurement of the 3PCF for a sample of 187 000 galaxies from the WiggleZ Dark Energy Survey (Drinkwater et al. 2010), which probes galaxies in the range $0.1 < z < 1.0$ with a median redshift $z \sim 0.6$. Using N-body simulations to study DM statistics, we estimate the WiggleZ galaxy bias and thereby measure σ_8. These estimations have been done in the past (Gaztañaga et al. 2005; Ross, Brunner & Myers 2006; Marín 2011; McBride et al. 2011b), but the fact that the WiggleZ survey spans such a large range of redshifts with a large overall volume allows us to split our galaxy sample into redshift slices and measure σ_8 as a function of redshift, hence constraining the large-scale structure growth history.

This paper is organized as follows. In Section 2, we describe our survey and the simulations we use; in Section 3 we introduce the galaxy 3PCF and how it is measured, along with the model connecting galaxy and DM clustering. In Section 4, we present the measurements of the WiggleZ 3PCF as a function of scale and shapes. In Section 5, we discuss constraints on the galaxy bias and σ_8 as a function of redshift. In Section 6, we summarize our findings. We note that a fiducial flat Λ cold dark matter (ΛCDM) cosmological model with matter density $\Omega_m = 0.27$ and Hubble parameter $H_0 = 100\,h\,\mathrm{km\,s^{-1}\,Mpc^{-1}}$ with $h = 0.7$ is used throughout this paper to convert redshifts to distances, which are measured in h^{-1} Mpc.

2 DATA AND SIMULATIONS

2.1 The WiggleZ Galaxy Survey

The WiggleZ Dark Energy Survey (Drinkwater et al. 2010) is a large-scale galaxy redshift survey performed over 276 nights with the AAOmega spectrograph (Sharp et al. 2006) on the 3.9 m Anglo-Australian Telescope. With a area coverage of 816 deg², this survey has mapped 240 000 bright emission-line galaxies over a cosmic volume of approximately 1 Gpc³.

Target galaxies in seven different regions were chosen using UV photometric data from the *GALEX* survey (Martin et al. 2005) matched with optical photometry from SDSS DR4 (Adelman-McCarthy et al. 2006) for regions in the Northern Galactic Cap (9 h, 11 h and 15 h), and from the Red-Sequence Cluster Survey 2 (RCS2; Gilbank et al. 2011) for those regions in the Southern Galactic Cap (0 h, 1 h, 3 h, 22 h). The selection criteria consisted of applying magnitude and colour cuts (Drinkwater et al. 2010) in order to select star-forming galaxies with bright emission lines with a redshift distribution centred around $z \sim 0.6$. The selected galaxies were observed in 1 h exposures using the AAOmega spectrograph, and their redshifts were estimated from strong emission lines.

To study the evolution of the bias and σ_8 with cosmological time, we use three overlapping redshift slices [0.1, 0.5], [0.4, 0.8] and [0.6, 1.0]. We estimate the effective redshift of each sample by averaging the redshifts of galaxy pairs at the distances covered by our study, i.e. from 10 to 100 h^{-1} Mpc; we find that the effective redshifts for the closest, middle and farthest slices are $z_{\mathrm{eff}} = [0.35, 0.55, 0.68]$, respectively. Table 1 shows the details of the samples used.

Fig. 1 shows the angular distribution of galaxies in the regions considered. We show the targets in RA, Dec. coordinates, where it can be seen that the angular completeness varies considerably

Table 1. Number of galaxies in WiggleZ regions used in this paper.

Redshift $z_{\rm eff}$	[0.1, 0.5] 0.35	[0.4, 0.8] 0.55	[0.6, 1.0] 0.68	JK subregions $N_i^{\rm JK}$
00 h	6601	10 698	8774	9
01 h	6038	9437	7880	8
03 h	6492	10 241	8756	8
22 h	13 508	16 146	11 024	15
09 h	10 106	18 978	11 424	12
11 h	13 603	23 940	13 919	16
15 h	14 517	30 015	19 471	20
All regions	74 440	119 455	81 248	88

Figure 2. Redshift distribution of WiggleZ galaxies. The thin lines correspond to the radial selection function for each individual angular region. The thick lines represent the redshift distribution of all WiggleZ galaxies (black), WiggleZ galaxies in the North Cap (blue) and WiggleZ galaxies in the South Cap (red).

between regions, due to masking of bright stars, the availability of input *GALEX* imaging, and differences in the accumulated observation time within each region and between regions. If not taken into account properly by modelling the angular selection function, these non-uniformities may lead to artificial structures, different from what we can expect from cosmic variance. Several studies, such as Gaztañaga et al. (2005), Nichol et al. (2006), McBride et al. (2011a) and Norberg et al. (2011), agree that higher order correlation functions are more sensitive to these effects than the two-point function. However, as we describe below in Section 3.2, we conclude that our modelling of the angular completeness is adequate to carry out our analyses.

Fig. 2 shows the redshift distribution of the different regions, peaking at $z \sim 0.6$, but extending to redshift $z \sim 1.0$. The variable number density with redshift determines the effective redshifts of our samples as measured above. It can also be seen that the average distribution of galaxies varies between regions.

This is partly explained by cosmic variance, but also the selection functions of SDSS and RCS2 galaxies differ considerably at low redshifts, owing to the available colours for galaxy selection from the input catalogues (Drinkwater et al. 2010). To deal with these
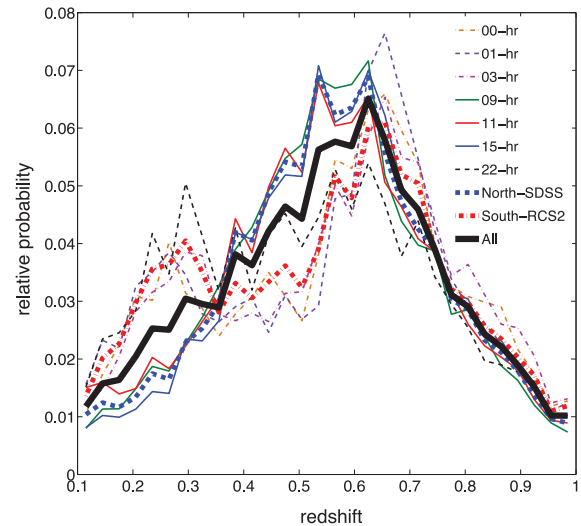
issues we model the angular coverage and redshift distributions in each survey region individually (Blake et al. 2010).

2.2 The GiggleZ simulations

In order to measure galaxy bias we need to model the underlying DM correlations. For the two-point functions, there exists a large amount of literature of models (e.g. Peebles 1980; Kaiser 1987; Bernardeau et al. 2002; Cooray & Sheth 2002; Smith et al. 2003, and references therein), but in the case of the higher order correlations, modelling
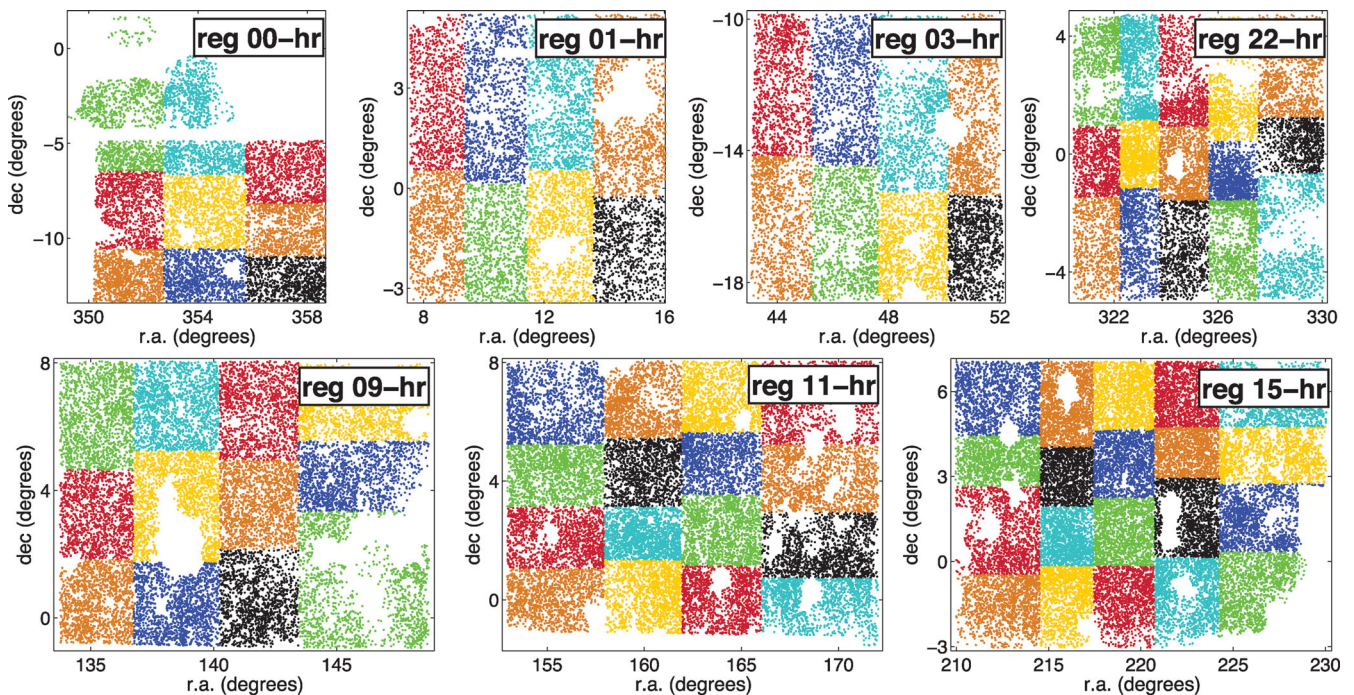

Figure 1. Angular distribution of WiggleZ galaxies. The top four regions correspond to those WiggleZ galaxies in the RCS2 footprint; the bottom three regions to the ones obtained using SDSS. Colours correspond to subregions containing the same effective area.

has focused mostly on the large-scale behaviour (e.g. Jing & Borner 1997; Bernardeau et al. 2002), although there have been efforts to model the non-linear, small scales (e.g. Yang, Mo & van den Bosch 2003; Fosalba, Pan & Szapudi 2005). Most importantly, for the 3PCF there is no satisfactory treatment of redshift-space distortions, although some attempts have been made for the bispectrum, the Fourier transform of the 3PCF, by Scoccimarro, Couchman & Frieman (1999) and Smith, Sheth & Scoccimarro (2008), which are valid for limited range of scales. Therefore, as has been done in previous works (Gaztañaga et al. 2005; Marín 2011; McBride et al. 2011b), we will obtain constraints on the galaxy bias and cosmological parameters by comparing the WiggleZ galaxy 3PCF with the DM correlations measured in *N*-body simulations, which include the full set of non-linear effects.

We measured the DM correlation functions using the Gigaparsec WiggleZ Survey simulations (GiggleZ; Poole et al., in preparation), which have been generated in support of WiggleZ science. In a 1 h^{-1} Gpc^3 periodic cube, 2160^3 DM particles with individual masses of $m_p = 7.5 \times 10^9\,h^{-1}\,M_\odot$ were evolved using a flat ΛCDM model, with cosmological parameters from *Wilkinson Microwave Anisotropy Probe* 5 (*WMAP*5) results (Komatsu et al. 2009). In order to compare the correlation functions of WiggleZ galaxies and DM, we measured them in snapshots of the simulation at the same effective redshifts as the WiggleZ subsamples.

DM haloes are identified in two steps (Springel et al. 2001): First, using a friends-of-friends algorithm with a linking length of $l = 0.2$ times the mean particle separation, bound structures are found (parent haloes). Secondly, given the high resolution of our simulation, we were able to find gravitationally bound substructures inside these parent haloes. From the main halo catalogue, we create subsets ordered by maximum circular velocity (which we use as a proxy for halo mass) with the same mean number density as the WiggleZ galaxies $n \sim 2.5 \times 10^{-4}\,(h^{-1}\,\mathrm{Mpc})^{-3}$. These halo catalogues are used to carry out consistency checks in our phenomenological model to estimate the bias and cosmological parameters.

3 THE GALAXY 3PCF

3.1 Definitions and methods

The galaxy *n*-point correlation functions are the average of correlated galaxy overdensity δ_{gal} measured at *n* different points (Peebles 1980). Whereas the 2PCF $\xi(r)$ allows us to estimate the probability of finding pairs with a separation *r*, the 3PCF $\zeta(r_1, r_2, r_3)$ describes the probability of finding triplets with galaxies as vertices. The joint probability of finding three objects in three infinitesimal volumes dV_1, dV_2 and dV_3 is given by the 'full' 3PCF (Peebles & Groth 1975; Peebles 1980),

$$P = [1 + \xi(r_1) + \xi(r_2) + \xi(r_3) + \zeta(r_1, r_2, r_3)]$$
$$\times \bar{n}^3 dV_1 dV_2 dV_3, \tag{1}$$

where $\bar{n}$ is the mean density of objects, ξ is the 2PCF and ζ is the reduced or 'connected' 3PCF. In other words, this means that the probability of finding galaxies in a particular triangular configuration has contributions from triplets found by random chance, plus contributions from correlated pairs plus the third point found at random (the ξ terms), and lastly by intrinsically correlated triplets (the ζ term). In the DM or galaxy field, the 2PCF and 3PCF are given by

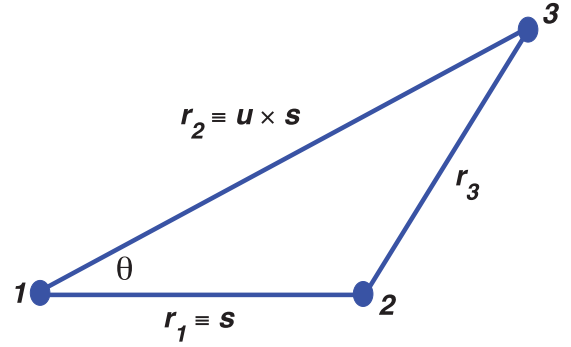$$\xi(r) = \langle \delta(\boldsymbol{x}_1)\delta(\boldsymbol{x} + \boldsymbol{r}) \rangle \tag{2}$$

Figure 3. Parametrization of triangles for calculation of correlation functions.

$$\zeta(r_1, r_2, r_3) = \langle \delta(\boldsymbol{x}_1)\delta(\boldsymbol{x}_2)\delta(\boldsymbol{x}_3) \rangle, \tag{3}$$

where δ is the fractional overdensity of objects (galaxies, haloes or DM particles) or the continuous field studied, and $\boldsymbol{x}_1$, $\boldsymbol{x}_2$ and $\boldsymbol{x}_3$ form a closed triangle (see Fig. 3). The triangle sides r_i are the distances between objects in the triplet; thus, the 3PCF depends upon the scales and shapes of spatial structures (Barriga & Gaztañaga 2002; Gaztañaga & Scoccimarro 2005; Sefusatti & Scoccimarro 2005; Marín et al. 2008). Since the ratio ζ/ξ^2 is both predicted on large scales from perturbation theory (Bernardeau et al. 2002) and measured to be close to unity over a large range of length scales, even though ξ and ζ each vary by orders of magnitude (Peebles 1980), we will often present results using the 'reduced' (or normalized) 3PCF,

$$Q(s, u, \theta) \equiv \frac{\zeta(s, u, \theta)}{\xi(r_1)\xi(r_2) + \xi(r_2)\xi(r_3) + \xi(r_3)\xi(r_1)}.$$

Here, $s \equiv r_1$ sets the scale size of the triangle, and the shape parameters are given by the ratio of two sides of the triangle, $u \equiv r_2/r_1$, and the angle between those two sides, $\theta = \cos^{-1}(\hat{r}_1 \cdot \hat{r}_2)$, where $\hat{r}_1$, $\hat{r}_2$ are unit vectors in the directions of those sides. The reduced 3PCF is also better suited for visualizing the growth of non-Gaussian structure and the shape dependence of clustering than ζ. On the other hand, on large scales, since $\xi \to 0$, the ratio ζ/ξ^2 becomes very unstable and its errors non-Gaussian, with the consequences of overestimating the covariances, diminishing the overall signal-to-noise ratio (S/N) and introducing a systematic deviation in the confidence intervals of the fitted parameters; therefore, we use ζ and not Q for model fits.

In this work, we measure correlation functions for triangles with base side $s = 10, 15, 20$ and $30\,h^{-1}$ Mpc, with the shape parameters $u = 1.0, 2.0, 3.0$ and 10 equally spaced bins in θ. In total, we measure correlations for 120 triangular configurations.

3.2 Measuring correlation functions

We measure first the 2PCF and 3PCF in each WiggleZ region (i.e. in angular and redshift cuts). For a particular WiggleZ region, we calculate the 2PCF using the estimator of Landy & Szalay (1993),

$$\xi = \frac{DD - 2DR + RR}{RR}. \tag{4}$$

Here, *DD* is the number of data pairs normalized by $N_D \times N_D/2$, *DR* is the number of pairs using data and random catalogues normalized by $N_D N_R$, and *RR* is the number of random pairs normalized by $N_R \times N_R/2$, where N_D and N_R are the number of points in the data

and in the random catalogue of the region, respectively. The 3PCF is calculated using the Szapudi & Szalay (1998) estimator

$$\zeta = \frac{DDD - 3DDR + 3DRR - RRR}{RRR}, \qquad (5)$$

where DDD, the number of data triplets, is normalized by $N_D^3/6$, and RRR, the random data triplets, is normalized by $N_R^3/6$. DDR is normalized by $N_D^2 N_R/2$ and DRR by $N_D N_R^2/2$. Due to the low density of our galaxies $n \sim 2.5 \times 10^{-4} \, h^3 \, \mathrm{Mpc}^{-3}$, we are limited by shot noise on these large scales and consequently the application of FKP weighting (Feldman, Kaiser & Peacock 1994) to the pair and triplet counts does not affect the results. To estimate the number of pairs and triplets, we use the NTROPY-NPOINT software, an exact n-point calculator which uses a kd-tree framework with true parallel capability and enhanced routine performance (Gardner, Connolly & McBride 2007; McBride et al. 2011a).

The random catalogues were built using the methods described by Blake et al. (2010), which estimate the angular and radial selection function of each survey region due to survey geometry and incompleteness in the parent photometry and spectroscopic follow-up. This modelling process produces a series of Monte Carlo random realizations of the angular and redshift catalogue in each region, which is used in our correlation function estimations. In this paper, we measure the 3PCF using 10 random catalogues for each region, with $N_R = 4N_D$ for each of the random catalogues for the intermediate scales ($s = 10, 15 \, h^{-1}$ Mpc), and $N_R = N_D$ for the largest scales ($s = 20, 30 \, h^{-1}$ Mpc).

For our choice of binning (resolution) of the triangles, we use the same scheme as Marín (2011) and McBride et al. (2011a): first, we select the central s, u and θ, and their corresponding side lengths in redshift space s_i, with $i = 1, 2, 3$. Then, to calculate the 2PCF and 3PCF, we accept triangles with sides in the range $(1 - 0.075)s_i < r_i < (1 + 0.075)s_i$, implying a 15 per cent binning resolution. This is a higher resolution than used for the LRGs (Marín 2011) but is justified by the higher number density of the WiggleZ galaxies.

In Fig. 4 we explore the effects of the radial and angular selection functions on the 2PCF and connected 3PCF ζ for a selection of con-

figurations ($s = 15, 20 \, h^{-1}$ Mpc, $u = 2$). Using a DM halo catalogue from the GiggleZ simulation that has a similar two-point clustering as our WiggleZ sample at $z = 0.55$, we create three different kinds of mock catalogues with the same geometry as the survey: the first group (red dashed line) does not include any radial or angular selection effects apart from the large-scale boundaries of the WiggleZ regions. The green (dot–dashed) lines denote measurements from mocks with the same radial selection function of WiggleZ galaxies at $z_{\mathrm{eff}} = 0.55$. The blue (solid) lines show mocks with the same angular and radial selection function of WiggleZ galaxies. In general, the measurements of the correlation functions using the different mocks are very similar, signalling that our selection functions and random catalogues allow us to recover the intrinsic correlations of the galaxy field.

3.3 Galaxy bias model

Since different types of galaxies form inside different DM haloes, they are an imperfect tracer of the overall DM distribution (Bardeen et al. 1986; Berlind & Weinberg 2002; Cooray & Sheth 2002), and their n-point correlations will differ as well. Many models of this galaxy bias have been proposed, and an accepted working model on large scales is the deterministic and local bias formalism, where we relate real-space galaxy overdensity δ_{gal} to the underlying matter density δ_{m} (Fry & Gaztanaga 1993; Frieman & Gaztanaga 1994):

$$\delta_{\mathrm{gal}} = b_1 \delta_{\mathrm{m}} + \frac{b_2}{2} \delta_{\mathrm{m}}^2 + \cdots \qquad (6)$$

up to second order, where δ_{gal} and δ_{m} are the local galaxy and matter overdensities smoothed over some scale R. To leading order, this bias prescription leads to a relation between the galaxy and matter 2PCF and connected 3PCF. Following Pan & Szapudi (2005), leading-order perturbation theory (Bernardeau et al. 2002) shows that if we fix all cosmological parameters except the overall amplitude of the initial spectrum of perturbations characterized by σ_8, then there is a degeneracy between the effect of this parameter and the bias on the two-point and three-point functions. The relations between matter and galaxy correlations in this model are

$$\xi_{\mathrm{gal}}(r) = (\sigma_8/\sigma_{8,\mathrm{fid}})^2 b_1^2 \xi_{\mathrm{m}}(r) \qquad (7)$$

$$\zeta_{\mathrm{gal}}(r_{12}, r_{23}, r_{31}) = (\sigma_8/\sigma_{8,\mathrm{fid}})^4 \Big[b_1^3 \zeta_{\mathrm{m}}(r_{12}, r_{23}, r_{31}) \\ + b_2 b_1^2 (\xi_{\mathrm{m}}(r_{12})\xi_{\mathrm{m}}(r_{23}) + \mathrm{perm.}) \Big]. \qquad (8)$$

In observations we measure the correlation functions in redshift space, where the 'real' correlations are distorted by peculiar velocities (with respect to the Hubble expansion), which on large scales depend on the growth rate of perturbations $f \approx \Omega_{\mathrm{m}}(z)^{0.55}$ and on galaxy bias. For the two-point function, we have that $\xi_{z\text{-space}} \sim f_2 \xi_{r\text{-space}}$, with (Kaiser 1987)

$$f_2 = 1 + \frac{2}{3}\left(\frac{f}{b_1}\right) + \frac{1}{5}\left(\frac{f}{b_1}\right)^2. \qquad (9)$$

In the case of the 3PCF, there is also an effect from redshift-space distortions of similar order (Scoccimarro et al. 1999). However, it depends not only on the linear bias and f, but also on the non-linear bias and the shape and scale parameters of the triangle observed. As mentioned before, analytical models of these distortions have been proposed for the bispectrum on large scales (Scoccimarro et al. 1999) where its validity is limited. On small, non-linear scales
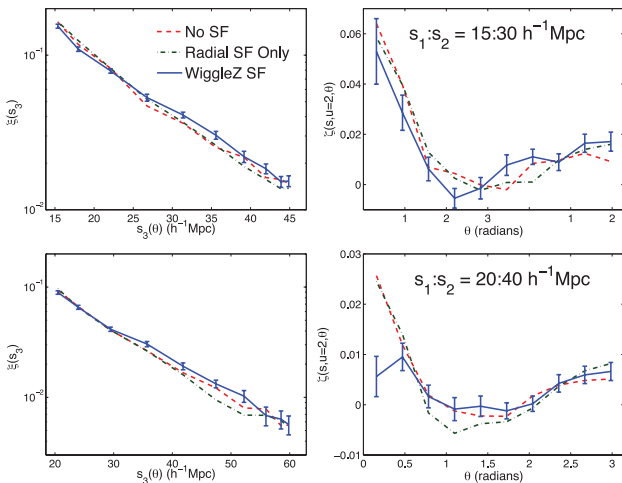

Figure 4. Correlation function measurements for a GiggleZ halo catalogue. Selecting a set of triangular configurations, with $s = 15 \, h^{-1}$ Mpc (top) and $s = 20 \, h^{-1}$ Mpc (bottom) and $u = 2$, we plot the redshift-space reduced 2PCF of the third side $\xi(s_3(\theta))$ (left-hand panels) and connected 3PCF, ζ (right-hand panels) of a selected DM halo catalogue from the GiggleZ simulation with similar clustering as WiggleZ galaxies, showing the effects of radial and angular selection functions.

(Smith et al. 2008) the transformation back to configuration space is challenging (six-dimensional integrals) and numerically intractable.

For these reasons we opt to use an empirical model that has been used by Pan & Szapudi (2005) and Gaztañaga et al. (2005) in analyses of the 2dFGRS galaxies. We use the *N*-body measurements of the correlation functions in redshift space in equations (7) and (8), replacing $\xi_{r\text{-space}} \to \xi_{z\text{-space}}$ and $\zeta_{r\text{-space}} \to \zeta_{z\text{-space}}$ at the different effective redshifts of our WiggleZ slices. Given the low S/N of the 3PCF measurements, this is justified by the fact that for low-bias tracers (such as the 2dFGRS galaxies studied in the papers mentioned above) with $b \sim 1$, $f_{2,b_1} \approx f_{2,b_1=1}$, with differences of the order of 10 per cent when $(b_1 - 1) = 0.3$, smaller than the statistical error in our measurements (of the order of 20–30 per cent); the impact of the constraints on σ_8 is slightly lower. Since we use *N*-body simulation measurements to compare to our galaxy correlations, the only cosmological parameter we modify is σ_8 through the ratio $\sigma_8/\sigma_{8,\text{fid}}$ in equations (7) and (8).

The justification of this model is illustrated by Fig. 5, where we take two halo samples (groups) from the GiggleZ simulation at redshift $z = 0.6$, with a similar number density as WiggleZ galaxies $n_h = 2.5 \times 10^{-4} \, (h^{-1} \, \text{Mpc})^{-3}$. The first sample, 'group 05', is composed of low-mass haloes, with clustering similar to that of WiggleZ galaxies, and the second sample, 'group 44', consists of very massive haloes. We measured their correlation functions in real space and then estimated their linear and non-linear bias parameters by comparison with the matter correlation functions measured in the GiggleZ simulation, using equations (7) and (8) for a fixed $\sigma_8(z = 0) = 0.812$ (see Section 5.1). In the case of the low-bias sample, $\chi^2_{r,\text{g05}}/\text{d.o.f.} = 0.87$, and for the high-mass sample $\chi^2_{r,\text{g44}}/\text{d.o.f.} = 0.96$. We then performed measurements in redshift space; we observe that in the case of the low-bias tracers, using the same bias in redshift space fits well their redshift-space 2PCF and 3PCF, with $\chi^2_{z,\text{g05}}/\text{d.o.f.} = 1.07$, but the same cannot be said for the high-mass haloes where $\chi^2_{z,\text{g44}}/\text{d.o.f.} = 22.44$. Since WiggleZ galaxies have a low linear bias $b_1 \sim 1$ (Blake et al. 2011b; Contreras et al. 2013),
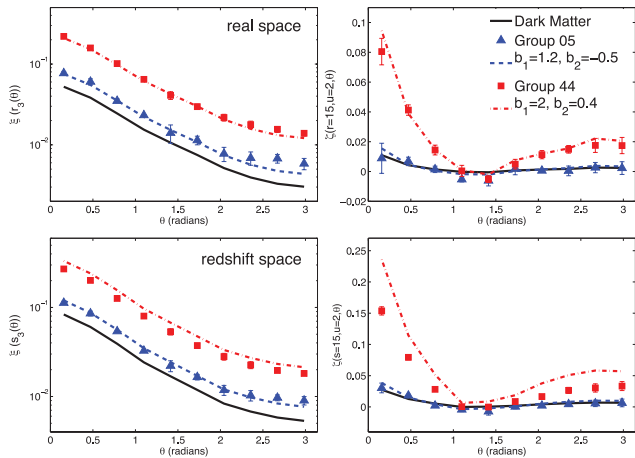
the approach we take is adequate for obtaining measurements of the linear and non-linear bias parameters and σ_8 as a function of redshift.

4 RESULTS

In this section we present the measurements of the 2PCF ξ, connected 3PCF $\zeta(s, u, \theta)$ and reduced 3PCF, $Q(s, u, \theta)$ of WiggleZ galaxies for a range of scales and shapes at different redshifts. We explore differences between regions, evolution with redshift, and our estimation of statistical errors and covariance.

4.1 Building the WiggleZ Survey correlations

In Fig. 6 we show the measurements of the correlation functions in the $z_{\text{eff}} = 0.55$ sample for each WiggleZ region. Measurements in different regions are consistent within the statistical errors from cosmic variance and shot noise. On these scales we notice how small differences in ξ and ζ translate to larger discrepancies in Q. The noisiest three-point functions are obtained in the smallest regions (in terms of volume), in this case the regions overlapping with the RCS2 survey.

We will build a 'combined' set of correlation functions calculated by optimally weighting individual contributions of the regions.

To measure the diagonal errors and covariance matrices, ideally we require a large number of mock galaxy catalogues whose correlation functions have similar amplitude and shape dependence to the one observed in our data. However, this is not currently tractable for WiggleZ galaxies due to their low bias, which would necessitate many high-resolution simulations in a cosmological volume. In past studies, we have used lognormal realizations (Blake et al. 2010) to generate a large number of mocks suited to match the WiggleZ two-point amplitudes. Unfortunately, by their construction (from generating points with a particular two-point distribution), these are not capable of reproducing the higher order clustering of galaxies.
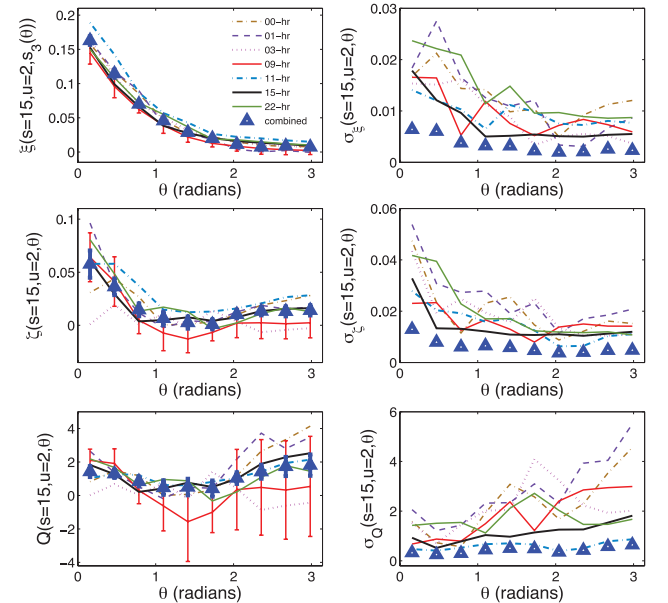

Figure 5. The 2PCF $\xi(s_3(\theta))$ (left) and connected 3PCF ζ (right) of two samples (groups) of haloes from the GiggleZ simulations in real space (top) and redshift space (bottom) at a snapshot $z = 0.6$. The black lines show results from the DM particles from the simulation, the blue triangles display measurements for a halo sample ('group 05') with average mass $4.8 \times 10^{11} \, h^{-1} \, \text{M}_\odot$ and the red squares show results for a halo sample ('group 44') with average mass $6.9 \times 10^{12} \, h^{-1} \, \text{M}_\odot$. The blue (short dashed) and red (dot dashed) lines denote biased DM for low-mass and high-mass haloes, respectively (bias parameters are listed in the figures).

Figure 6. The 2PCF $\xi(s_3)$ (top left), the connected 3PCF ζ (middle left) and the reduced 3PCF Q (bottom left) of each WiggleZ region in the $z_{\text{eff}} = 0.55$ slice, for triangles with $s_1 = 15 \, h^{-1} \, \text{Mpc}$ and $u = 2$. In the right-hand plots, we show the corresponding diagonal errors.

In this work, error measurements in each region are calculated from jack-knife (JK) resampling (Zehavi et al. 2005; McBride et al. 2011a; Norberg et al. 2011). In this method, we divide the whole volume of the sample in identical subsamples $i = 1, \ldots, N$, and we then measure correlation functions for the whole volume minus the ith subsample N times to get a set of N correlated measurements. In our case, in all WiggleZ regions we take subregions of equal area (weighted by sky completeness), with an equivalent physical size of approximately $120 \times 150 \times 900$ $(h^{-1}$ Mpc$)^3$ at $z = 0.55$. The angular cut has the same area independent of region, as can be seen in Fig. 1; thus, some WiggleZ regions have more JK subregions than others, depending on their total area coverage.

In order to obtain the JK variance in each region, we measure each X_i statistic (where X_i can be the 2PCF or the 3PCF), subtracting one of the JK subregions in turn. Then, we calculate the variance $\sigma_{X_i}^2$ of the individual WiggleZ region as

$$\sigma_{X_i}^2 = \frac{N_i^{\mathrm{JK}} - 1}{N_i^{\mathrm{JK}}} \sum_{j=1}^{N_i^{\mathrm{JK}}} \left(X_{i,j}^2 - \langle X_i \rangle^2 \right), \qquad (10)$$

where N_i^{JK} is the number of jack-knife subsamples, in region i (see Table 1). Then, we calculate the correlations in the overall survey using inverse-variance weighting. For the statistic X_{comb}, this is calculated as

$$X_{\mathrm{comb}} = \left(\sum_{i=1}^{N_{\mathrm{reg}}} \frac{1}{\sigma_{X_i}^2} \right)^{-1} \left(\sum_{i=1}^{N_{\mathrm{reg}}} \frac{X_i}{\sigma_{X_i}^2} \right), \qquad (11)$$

where $\sigma_{X_i}^2$ is the variance of the statistic in the WiggleZ subregion (calculated in equation 10), taken from the JK resampling method. $N_{\mathrm{reg}} = 7$ is the number of WiggleZ regions we use for the calculation of the combined correlations. We do this for ξ, ζ and Q. In principle, there should be no difference between calculating correlations using this method and measuring triplet counts across the whole survey; in practice, our method is more computationally efficient and gives us extra systematics tests by allowing us to compare results region by region.

Overall diagonal errors and covariance matrices are calculated by JK resampling the whole set of survey regions (see Fig. 1). In this way, we produce a catalogue of $N_{\mathrm{tot}}^{\mathrm{JK}} = 88$ measurements. The variance of the correlations is calculated as

$$\sigma_{X_{\mathrm{comb}}}^2 = \frac{N_{\mathrm{tot}}^{\mathrm{JK}} - 1}{N_{\mathrm{tot}}^{\mathrm{JK}}} \sum_{j=1}^{N_{\mathrm{tot}}^{\mathrm{JK}}} \left(X_j^2 - \langle X \rangle^2 \right). \qquad (12)$$

We also use this method to calculate the covariance matrix, which is used in the maximum likelihood approach to measure the galaxy bias and cosmological parameters.

4.2 The combined WiggleZ 3PCF

Fig. 7 shows the measurements of the redshift-space 2PCF $\xi(s_3(s, u, \theta))$, connected 3PCF $\zeta(s_1, s_2, \theta)$ and reduced 3PCF $Q(s_1, s_2, \theta)$ of WiggleZ galaxies (from optimally combining the seven independent regions) in all redshift slices for a range of scales $s_1 = 10, 15, 20$
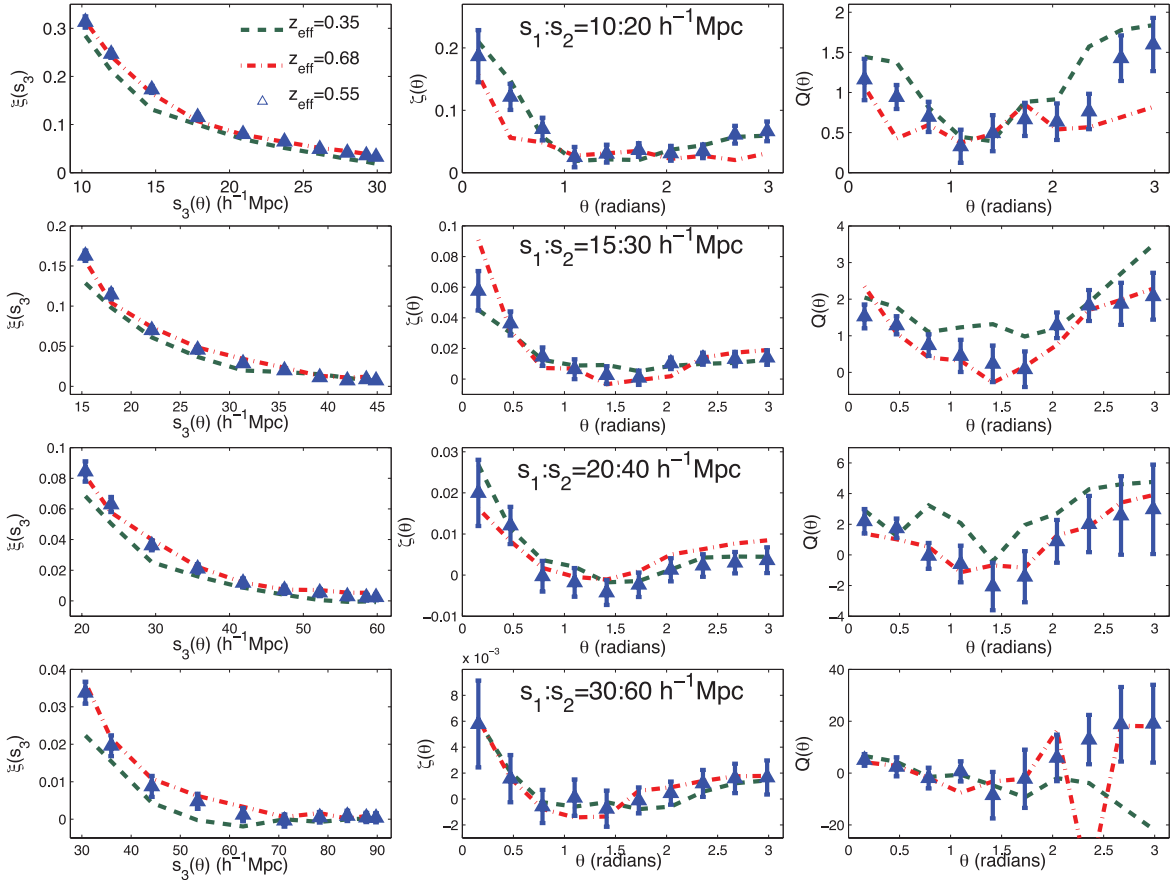

Figure 7. The combined redshift-space 2PCF $\xi(s_3(\theta))$ (left), connected 3PCF $\zeta(s, u = 2, \theta)$ (middle) and reduced 3PCF $Q(s, u = 2, \theta)$ (right) of WiggleZ galaxies in the $z_{\mathrm{eff}} = 0.55$ slice (blue triangles and error bars), in the slice at $z_{\mathrm{eff}} = 0.35$ (green dashed line) and in the $z_{\mathrm{eff}} = 0.68$ slice (red dash–dotted line). Different rows cover the range of scales of the triangles. Errors have been determined by JK resampling.

and 30 h^{-1} Mpc and shape $u = 2$ as a function of θ. We have additionally measured the correlations using $u = 1$ and 3, for a total of 120 configurations, which are shown in Appendix A.

We note qualitatively that we recover the same shape dependence of the galaxy 3PCF (mostly noticeable when looking at Q) which has been observed for galaxies at low redshift (Marín 2011; McBride et al. 2011a), namely a bigger 3PCF amplitude at small and large θ, i.e the collapsed and elongated configurations. This 'V-shape' is more prominent for large scales and elongated shapes; it is a consequence of the morphology of galaxy structures varying from spherically shaped clusters and groups on small $\sim 1 \, h^{-1}$ Mpc scales to filaments on the largest scales. This shape dependence of the 3PCF depends on the galaxy type under investigation. It has been observed in SDSS (Kayo et al. 2004; McBride et al. 2011a) and 2dFGRS (Gaztañaga et al. 2005) that L_* blue galaxies tend to have small 3PCF amplitudes on small scales and very pronounced V-shapes on large scales, compared to red galaxies and to $L > L_*$ galaxies, such as LRGs (Marín 2011). However, at a different redshift, we find that the shape dependence of the WiggleZ 3PCF agrees with these lower redshift measurements.

We also note that on larger scales the behaviour of the reduced 3PCF $Q(\theta)$ for the most elongated shapes is more erratic, specially for the $z = 0.35$ and 0.68 slices. This is due to the fact that as $\xi \to 0$ on large scales, the measurements of Q are less robust and its errors become non-Gaussian. But if we turn to analyse ζ instead, we can see that it is adequately measured up to the largest scales shown here, $s_3 \sim 100 \, h^{-1}$ Mpc.

Comparing the clustering signal in different redshift slices, we can see that in general the differences in the 3PCF are small and the signal is weaker than in the case of the central $z_{\mathrm{eff}} = 0.55$ slice. This does not necessarily indicate that there is no evolution of the clustering of WiggleZ galaxies with redshift; the underlying DM clustering changes with redshift, and consequently the linear and non-linear bias factors evolve. From the 2PCF measurements we can estimate the evolution of the linear bias, and using the 3PCF we can also test if there is evolution in the non-linear bias parameter.

In Fig. 8, we illustrate how the errors in our measurements vary with redshift by showing the 1σ diagonal errors (from JK resampling) of the 2PCF and 3PCF measurements for a selection of configurations ($s = 15, 20 \, h^{-1}$ Mpc and $u = 2$) of our (combined)
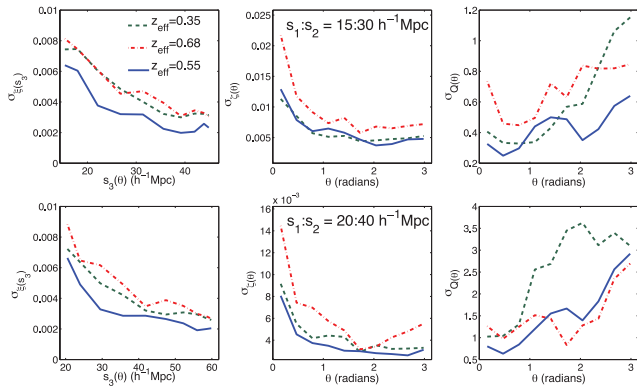

Figure 9. The correlation matrix of the WiggleZ 2PCF and 3PCF of triangles with $s_1 = 15 \, h^{-1}$ Mpc with $u = 1$, 2 and 3. Each element of the matrix is the covariance of each s, u and θ triplet.

redshift samples. It can be clearly seen that measurements are more accurate in the central redshift slice ($z_{\mathrm{eff}} = 0.55$) than in the outer ones. In these configurations, the relative error in the 2PCF is around $\sigma_\xi/\xi \sim 0.15$, and for the connected 3PCF ζ the relative errors reach $\sigma_\zeta/\zeta \sim 0.5$ in the central redshift slice.

4.3 Covariance estimation

We estimate the correlations between measurements of the 2PCF ξ and 3PCF ζ by empirically calculating the covariance matrix. Using the JK method, given a number of measurements N_{JK} in number of bins N_{b}, a fractional error of a quantity X for the sample k can be written as

$$\Delta_i^k = \frac{X_i^k - \langle X_i \rangle}{\sigma_{X_i}}, \tag{13}$$

where in our case, if $i \leq N_{\mathrm{b}}$, then $X = \xi(s_3)$ and otherwise $X = \zeta(s_1, s_2, s_3(\theta))$, and σ_{X_i} is the standard error on X_i calculated using the JK method. Then we calculate the correlation matrix (covariance matrix normalized by diagonal errors) as

$$C_{ij} = \frac{1}{N_{\mathrm{JK}}} \sum_{k=1}^{N_{\mathrm{JK}}} \Delta_i^k \Delta_j^k. \tag{14}$$

As an example that shows the observed behaviour of all configurations at different redshift samples, we show in Fig. 9 the correlation matrix of both $\xi(s_3(\theta))$ and $\zeta(\theta)$ for the configurations with $s = 15 \, h^{-1}$ Mpc, and $u = 1$, 2 and 3. In this case, the number of bins $N_{\mathrm{b}} = 30$, making C_{ij} a 60×60 matrix. We divide this matrix into four regions depicting the auto- and cross- correlations. In the case of the $\xi(s_3) - \xi(s_3)$ covariance, we notice that although it is dominated by diagonal terms, the off-diagonal terms are important too; the black stripes (signalling high covariance) in the off-diagonal matrices ($\xi(u_1, s_3) - \xi(u_2, s_3)$ where $u_1 \neq u_2$) correspond to triangles that share a similar s_3. The ζ-correlation matrix also shows important non-diagonal elements that are more correlated for the elongated shapes (a combination of true covariance and binning). The $\xi(s_3) - \zeta$ cross-covariance is small but needs to be considered in the analysis.

5 CONSTRAINTS ON GALAXY BIAS AND σ_8

We compare the DM correlations measured in the GiggleZ simulations to the WiggleZ 2PCF and 3PCF in order to constrain the

Figure 8. Diagonal errors of the correlation functions from JK resampling. Top: errors for the $s = 15 \, h^{-1}$ Mpc, $u = 2$ triangles for the 2PCF σ_ξ (left), connected 3PCF σ_ζ (centre) and reduced 3PCF σ_Q (right); the solid line corresponds to measurements in the $z_{\mathrm{eff}} = 0.55$ slice, the dashed line for the $z = 0.35$ slice and the dot–dashed line for the $z = 0.68$ slice. Bottom: same quantities for the $s = 20 \, h^{-1}$ Mpc, $u = 2$ triangles.
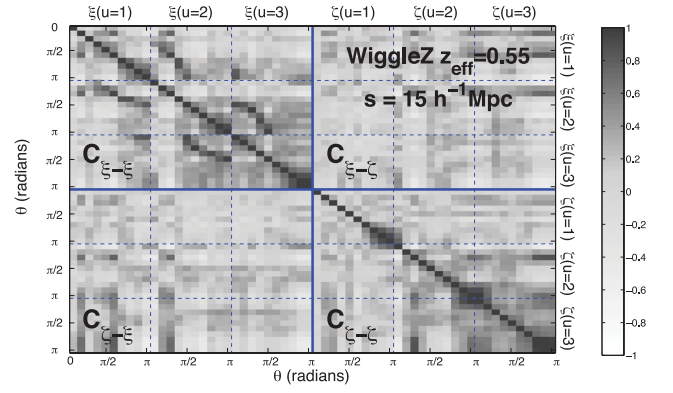
linear and non-linear bias parameters using the local bias model described in Section 3.3. In this analysis, we assume that all cosmological parameters are fixed, and fitted for $\sigma_8(z)$ by scaling the amplitude of the DM correlations in the manner of equations (7) and (8), with all quantities measured in redshift space. We want to emphasize that since we use N-body simulation measurements to compare to our galaxy correlations, and not an analytical model, the only cosmological parameter we can modify is $\sigma_8(z)$ through the ratio $\sigma_8/\sigma_{8,\,\mathrm{fid}}$, where the fiducial value corresponds to the one used in the GiggleZ simulation $\sigma_{8,\,\mathrm{fid}}(z=0) = 0.812$.

5.1 Methods

We carry out a maximum likelihood parameter estimation test, where we look to minimize the quantity

$$\chi^2 = \sum_{i=1}^{i=2N_b}\sum_{j=1}^{j=2N_b} \Delta_i\, C_{ij,\mathrm{SVD}}^{-1}\, \Delta_j, \tag{15}$$

where N_b is the number of triangular configurations used. We have N_b distances where we measure the 2PCF of s_3 and N_b triangles where we measure the 3PCF; therefore, we have $(2N_b)^2$ elements in our covariance matrix. The value of Δ_i is the difference between the correlation measured and the biased DM correlation:

$$\Delta_i = \left(\xi(s_3)_i^{\mathrm{obs}} - \xi(s_3)_i^{\mathrm{model}}\right)/\sigma_{\xi(s_3)i}, \quad \text{for } i \leq N_b, \tag{16}$$

$$\Delta_i = \left(\zeta(s,u,\theta)_i^{\mathrm{obs}} - \zeta(s,u,\theta)_i^{\mathrm{model}}\right)/\sigma_{\zeta(i)}, \quad \text{for } i > N_b, \tag{17}$$

where ξ^{model} and ζ^{model} are given by equations (7) and (8).

In order to invert the covariance matrix we use the approach of Gaztañaga & Scoccimarro (2005) and repeated in several 3PCF works (Gaztañaga et al. 2005; Marín 2011; McBride et al. 2011a), of employing only the highest eigenmodes of the covariance matrix to minimize effects of numerical noise. We employ the singular value decomposition (SVD) method, where our normalized covariance matrix can be decomposed $\mathbf{C} = \mathbf{U}\mathbf{D}\mathbf{V}^{\mathrm{T}}$ (and where $\mathbf{V} = \mathbf{U}$ for a symmetric matrix), where the diagonal matrix $D_{ij} = \lambda_i^2\delta_{ij}$ stores the eigenvalues in decreasing order, and the columns of the matrix $\mathbf{U}$ store the eigenmodes of $\mathbf{C}$. When inverting the matrix $\mathbf{C}^{-1} = \mathbf{V}\mathbf{D}^{-1}\mathbf{U}^T$ (where $D_{ij}^{-1} = (1/\lambda_i^2)\delta_{ij}$) we need to discard some of these eigenmodes, meaning set some $D_{ii}^{-1} \equiv 0$. First, we use a finite number of JK samples to estimate our covariance. Since using JK samples assumes the statistical independence of the subsamples, the JK regions should have a larger spatial extent than the largest scales studied. In our case, we use $N_{\mathrm{JK}} = 88$ JK regions because our largest scales are of the order of $\sim 100\,h^{-1}$ Mpc. However, we use a large number of 2PCF and 3PCF measurements, and generally $N_{\mathrm{JK}} < N_b$, which will make our matrix singular for modes $i > N_{\mathrm{JK}} - 1$ (see Press et al. 1992 for instance). Therefore, all those eigenmodes have to be discarded. A second cut comes from the fact that even though the covariance matrix is not singular when the first cut is applied, there are still eigenvalues λ_i^2 with very low numerical value, which will make unstable the inversion of C_{ij} with $\lambda_i^2 < \sqrt{2/N_{\mathrm{JK}}}$ (Gaztañaga & Scoccimarro 2005). Adding these unstable modes, as explained by these authors and later in Section 5.2, is equivalent to introducing artificial 'signal' to our measurements that will bias our fits.

We also have to set the minimum and maximum scale of the model fit. In our analysis this means that we choose configurations with the third size in a range $s_3 = [s_{3,\,\mathrm{min}}, s_{3,\,\mathrm{max}}]$. The minimum scale is given by the range of validity of the local bias model. The
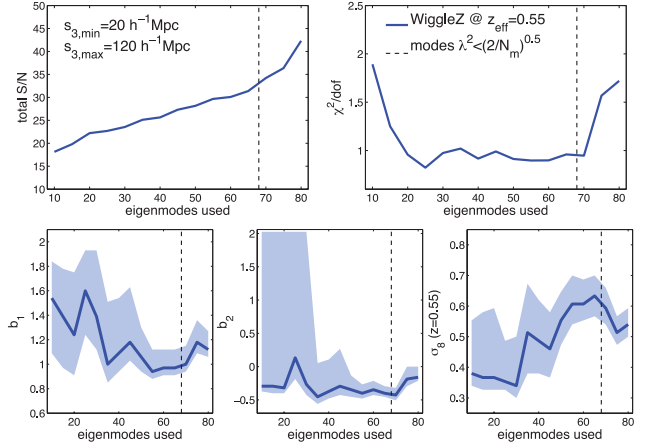

Figure 10. Dependence of the best-fitting bias parameters and σ_8 on the number of eigenmodes used for the $z_{\mathrm{eff}} = 0.55$ 2PCF and 3PCF analysis. In the left-hand panel, we show eigenmodes used after SVD (from the $\lambda_i^2 > \sqrt{2/N_{\mathrm{JK}}}$ limit), with fixed $s_{3,\,\mathrm{min}} = 20$ and $s_{3,\,\mathrm{max}} = 120\,h^{-1}$ Mpc. The top-left panel shows the total S/N according to equation (18) as a function of number of eigenmodes used. The top-right panel shows the χ^2/d.o.f., and lower panels show the 68 per cent CL intervals for b_1, b_2 and σ_8. The vertical dashed line represents the eigenmode limit where $\lambda_i^2 = \sqrt{2/N_{\mathrm{JK}}}$, with $N_{\mathrm{JK}} = 88$.

maximum scale could be set by systematics in the selection function or when the correlation signal is weak. In Figs 10–12, we show how our choices of the number of eigenvalues used, the values of $s_{3,\,\mathrm{min}}$ and $s_{3,\,\mathrm{max}}$, respectively, affect our constraints for our $z_{\mathrm{eff}} = 0.55$ sample.

We wish to make a sensible default choice for these options and establish that our essential conclusions are not very sensitive to this choice. Fig. 10 investigates the dependence of our results on the number of eigenmodes included, fixing $s_{3,\,\mathrm{min}} = 20\,h^{-1}$ Mpc and $s_{3,\,\mathrm{max}} = 120\,h^{-1}$ Mpc. We observe that if we use a small number of eigenvalues, we have large variations in the best-fitting values and poor constraints, especially in b_2; there is a range when the number of eigenvalues used is ~ 50 where our results are insensitive,
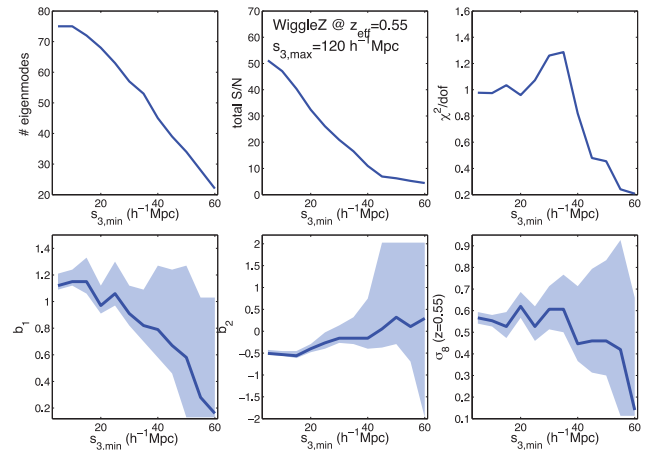

Figure 11. Dependence of the best-fitting bias parameters and σ_8 on the fitting range $s_{3,\,\mathrm{min}}$, with $s_{3,\,\mathrm{max}} = 120\,h^{-1}$ Mpc for the $z_{\mathrm{eff}} = 0.55$ 2PCF and 3PCF analysis. The top-left panel shows the number of eigenmodes used where $\lambda_i^2 = \sqrt{2/N_{\mathrm{JK}}}$ as a function of $s_{3,\,\mathrm{min}}$. The top-middle panel shows the total S/N, top-right panel the χ^2/d.o.f. of the best-fitting parameters. The lower panels show the 68 per cent CL intervals for b_1, b_2 and σ_8.
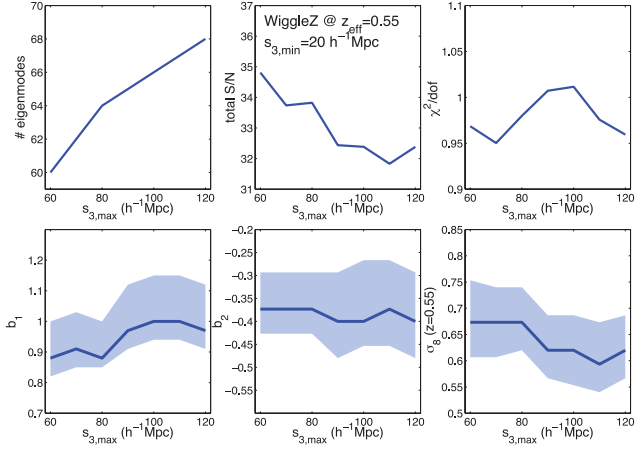
Figure 12. Same as Fig. 11, in this case fixing $s_{3,\,\mathrm{min}} = 20\,h^{-1}$ Mpc and having quantities shown as a function of $s_{3,\,\mathrm{max}}$.

and when we include modes with $\lambda_i^2 > \sqrt{2/N_{\mathrm{JK}}} \sim 65$ we again have unstable behaviour. In this figure, we also consider the dependence of the minimum χ^2 per degree of freedom on the number of eigenmodes employed, where the degrees of freedom are equal to the eigenmodes used minus the number of parameters we seek to constrain. We note that good fits are produced for a wide range of choices. We can also estimate the total S/N of the modes used as (Gaztañaga & Scoccimarro 2005)

$$\left(\frac{S}{N}\right)_i = \frac{1}{\lambda_i} \sum_{j=1}^{j=2N_{\mathrm{b}}} U_{ji} \frac{X_j}{\sigma_{X_j}}, \tag{18}$$

where $X_j = \xi_j$ when $j < N_{\mathrm{b}}$, and $X_j = \zeta_{j-N_{\mathrm{b}}}$ when $j > N_{\mathrm{b}}$.

Our conclusion from this analysis is that any systematic fluctuations in our parameter measurements do not dominate the statistical errors for a wide range of choices. Our default fits are performed for an eigenmode cut $\lambda_i^2 = \sqrt{2/N_{\mathrm{JK}}}$ and a fitting range between $s_{3,\,\mathrm{min}} = 20$ and $s_{3,\,\mathrm{max}} = 120\,h^{-1}$ Mpc for the $z_{\mathrm{eff}} = 0.55$ and 0.68 slices, and $s_{3,\,\mathrm{max}} = 100\,h^{-1}$ Mpc for the $z_{\mathrm{eff}} = 0.35$ sample.

Another aspect to consider in our analysis is that the measured redshifts in our survey contain a small fraction of 'redshift blunders'

(Blake et al. 2010), failures that tend to wash out the clustering we measure in our galaxy field. This redshift blunder fraction is $f_{\mathrm{b}} = 0.03$ for the $z_{\mathrm{eff}} = 0.35$ and 0.55 slices, and $f_{\mathrm{b}} = 0.05$ for the outer $z_{\mathrm{eff}} = 0.68$ slice; the correction to the 2PCF (since $\xi \propto \langle \delta_{\mathrm{gal}} \delta_{\mathrm{gal}} \rangle$) is to multiply the data and errors by $(1 - f_{\mathrm{b}})^{-2}$, meaning that the clustering amplitude increases, and the correction to the three-point function (where $\zeta \propto \langle \delta_{\mathrm{gal}} \delta_{\mathrm{gal}} \delta_{\mathrm{gal}} \rangle$) is $(1 - f_{\mathrm{b}})^{-3}$.

5.2 Constraints at $z_{\mathrm{eff}} = 0.55$

In Fig. 13, we show the measurements of b_1, b_2 and σ_8 in the $z_{\mathrm{eff}} = 0.55$ slice.

The measured linear bias, $b_1 \sim 1$, agrees with values obtained for WiggleZ galaxies using other methods (Blake et al. 2011b; Contreras et al. 2013), using two-point statistics, where in our study we additionally marginalize over all values of σ_8. We detect a significantly non-zero value for the non-linear bias $b_2 \sim -0.4$.

We measure the amplitude of fluctuations $\sigma_8(z)$ with 10 per cent accuracy and find that our results agree with independent predictions, based on cosmological parameter measurements from the CMB in a ΛCDM model. It is important to note that these estimates are independent of any other observable than the galaxy clustering itself. Extrapolated to $z = 0$, our measurements of σ_8 from WiggleZ galaxies are consistent with conclusions from 3PCF measurements of other tracers such as the LRGs (Marín 2011), which provides evidence that this method is robust against the type of galaxy used.

As is shown in Table 2, the empirical bias model is an adequate fit to the data, and that can be graphically seen in the right-hand

Table 2. Constraints on bias parameters and σ_8 for WiggleZ samples.

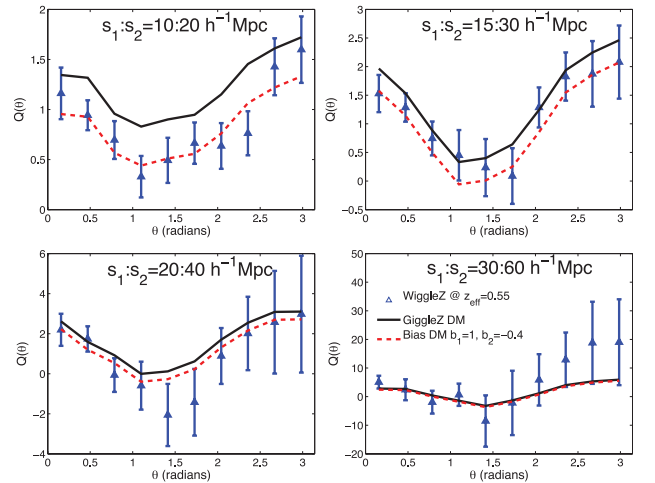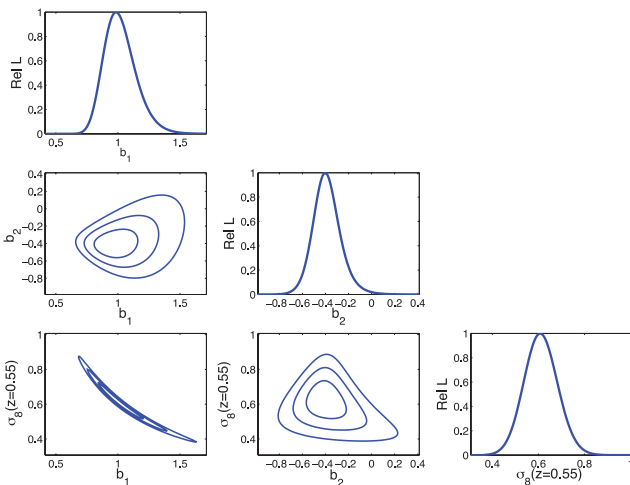| z_{eff}	b_1	b_2	σ_8	χ^2/d.o.f.	S/N
0.35	$0.72^{+0.14}_{-0.14}$	$-0.36^{+0.11}_{-0.08}$	$0.69^{+0.12}_{-0.11}$	1.10	3.25
0.55	$0.99^{+0.10}_{-0.09}$	$-0.41^{+0.09}_{-0.08}$	$0.61^{+0.06}_{-0.05}$	0.96	4.99
0.68	$1.06^{+0.16}_{-0.18}$	$-0.48^{+0.14}_{-0.12}$	$0.53^{+0.08}_{-0.07}$	0.82	4.62

Figure 13. Left: constraints on the bias parameters b_1, b_2 and σ_8 for the $z_{\mathrm{eff}} = 0.55$ WiggleZ redshift slice. The contours represent 1σ, 2σ and 3σ joint confidence regions for a two-parameter fit. Right: DM reduced 3PCF (black thick line), the WiggleZ $Q(\theta)$ for the $z_{\mathrm{eff}} = 0.55$ slice and the biased DM $Q(\theta)$ (dashed line) using the best-fitting parameters found in this analysis.

plots of Fig. 13, where we show the biased DM $Q(\theta)$, which in our model depends on the bias parameters but not on σ_8:

$$Q_{gal} = \frac{1}{b_1}\left(Q_m + \frac{b_2}{b_1}\right). \qquad (19)$$

We can see that our galaxy bias model is adequate on all scales, but our fits are mainly driven by the $s = 10$ and $15\ h^{-1}$ Mpc configurations, which have the highest S/N.

5.3 Constraints at different redshifts

We repeated the analysis of the correlation functions for the other two redshift slices in order to get constraints on the bias parameters and σ_8 as a function of redshift. In Table 2 we show our results. In general, we can see that there is a clear trend in all the parameters with redshift, and that from the values of $\chi^2/d.o.f.$, our model of the bias provides a good fit. We also estimated the covariance between the best-fitting parameters in different redshift slices, expected due to the overlap between redshift samples. In order to make this measurement we fitted the bias parameters and σ_8 to each delete-1 JK sample, obtaining $N_{JK} = 88$ sets of best-fitting parameters which we used to construct a covariance matrix. We show the correlation matrix of these parameters in Fig. 14. We observe that in any individual redshift slice there is
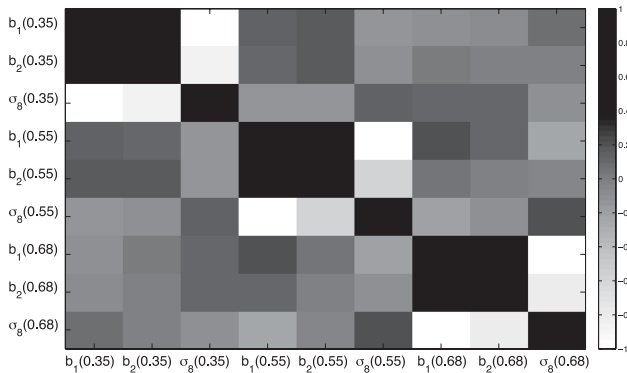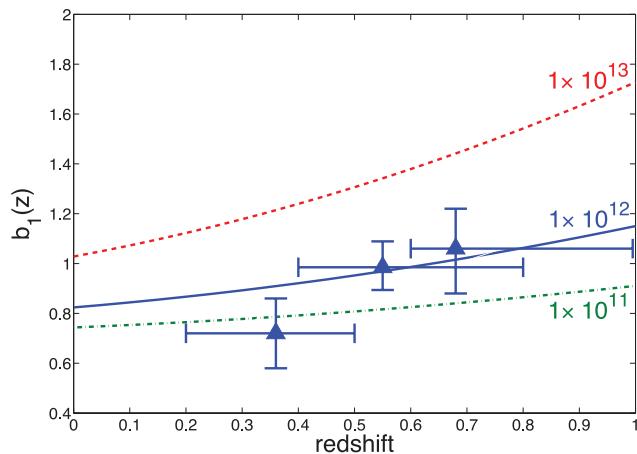
a positive correlation between b_1 and b_2 and a negative correlation between these parameters and σ_8. Although there is overlap in the redshifts of the samples studied, the correlation coefficients between the best-fitting parameters in separate redshift slices are small.

In the following, we study the change of the bias parameters and $\sigma_8(z)$ with redshift in more detail.

5.3.1 Constraints of WiggleZ bias

Fig. 15 displays the change of the galaxy bias with redshift. Due to our selection criteria, we are not necessarily selecting the same population of galaxies at different redshifts (Li et al. 2012), specially at redshifts $z < 0.5$. Therefore, we only can make general statements about evolution of the bias of WiggleZ galaxies. For the linear bias b_1, it can be seen that there is an upward trend of bias with redshift, consistent with what is expected for the evolution of haloes of a given mass: massive objects are less common in older times, and therefore more biased.

In order to compare our measured bias evolution to the expectation of simple models, we also plot the evolution of the bias of DM haloes of fixed mass with redshift in the halo model. These are given by the analytical expectation using Sheth–Tormen mass functions (Sheth, Mo & Tormen 2001) for the DM haloes, and the linear and non-linear bias from the work of Scoccimarro et al. (2001). Since our galaxies are a subsample of the total population, with a particular colour and luminosity selection, we do not expect that they should follow exactly one track of evolution, but in any case, our measured bias evolution seems to agree with those galaxies living in haloes with masses $\sim 10^{12}\ h^{-1}\ M_\odot$.

In our measurements and in the halo model, it is expected that when a galaxy tracer has a linear bias ~ 1, it should have a small but significantly negative non-linear bias b_2. In the right-hand panel of Fig. 15, we show the evolution of the WiggleZ galaxies' non-linear bias. These have negative values, and their trend agrees with what is expected of $\sim 10^{12}\ h^{-1}\ M_\odot$ haloes. A more detailed analysis using halo occupation distribution models is needed to have a complete picture of how WiggleZ galaxies populate DM haloes; this is beyond the scope of this paper.
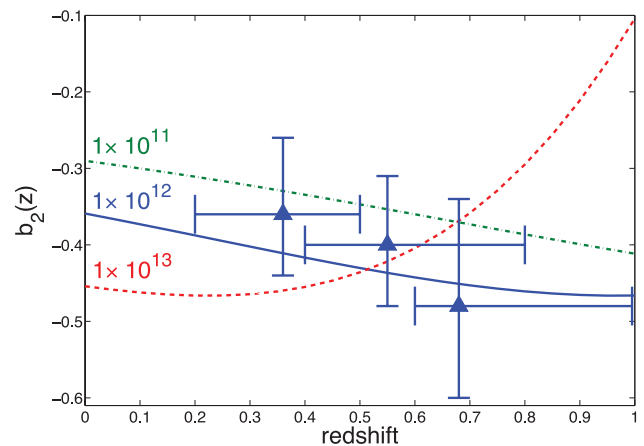

Figure 14. Correlation matrix of WiggleZ best-fitting parameters b_1, b_2 and σ_8 as a function of redshift.

Figure 15. Evolution of the bias parameters. Left: evolution of linear bias: triangles denote best-fitting parameters from our WiggleZ regions. Lines show halo model prediction of bias for haloes of masses $M_h = 10^{11}$ (green dash–dotted line), 10^{12} (blue solid line) and $10^{13}\ h^{-1}\ M_\odot$ (red dashed line). Right: evolution of the non-linear bias parameters.

5.3.2 *Evolution of cosmic growth*

In Fig. 16 we plot our measurements of σ_8 as a function of redshift from the WiggleZ survey data. In linear theory, the value of σ_8 is calculated as

$$\sigma^2(R = 8, z) = \int \frac{\mathrm{d}^3 k}{(2\pi)^3} |W(k, R = 8)|^2 P_{\mathrm{lin}}(k, z), \qquad (20)$$

where $W(k, R)$ is the Fourier transform of a top-hat window of radius $R = 8\,h^{-1}$ Mpc. The linear power spectrum evolves as $P_{\mathrm{lin}}(k, z) \propto [D(z)/D(z_*)]^2 P(k, z_*)$, where z_* is a reference redshift (e.g., the redshift of recombination) and $D(z)$ is the linear growth factor, obtained from the solution to the linearized equations of motion of primordial overdensities (Peebles 1980; Bernardeau et al. 2002). The evolution of the linear growth factor depends on the parameters of the cosmological model (Lahav & Suto 2004). Thus, we obtain

$$\sigma_8(z) = \frac{D(z)}{D(z = 0)} \sigma_8(z = 0). \qquad (21)$$

Therefore, $\sigma_8(z)$ measurements from the 2PCF and 3PCF can be used to study the evolution of the linear growth factor.

As predicted by the standard cosmological model, the value of $\sigma_8(z)$ we measure decreases at earlier times, in agreement with the *WMAP*5 cosmological parameters. Assuming a flat ΛCDM model with $\Omega_m = 0.27$ we find that when extrapolated to the present epoch, $\sigma_8(z = 0) = 0.79^{+0.06}_{-0.07}$. Our results also agree with the latest estimation of $\sigma_8(z)$ using BOSS/SDSS-LRG passive galaxies from Tojeiro et al. (2012); modelling the evolution of the linear bias for their particular population they find similar values to ours. However, in our work we need to make no assumptions about the evolution of the bias, just in the validity (range of scales) of the empirical bias model we adopt. We also find agreement with other measurements of σ_8 from the 3PCF of the SDSS LRG sample (Marín 2011); they find $\sigma_8(z = 0.35) = 0.65^{+0.02}_{-0.05}$, consistent with our measurements at the same effective redshift.
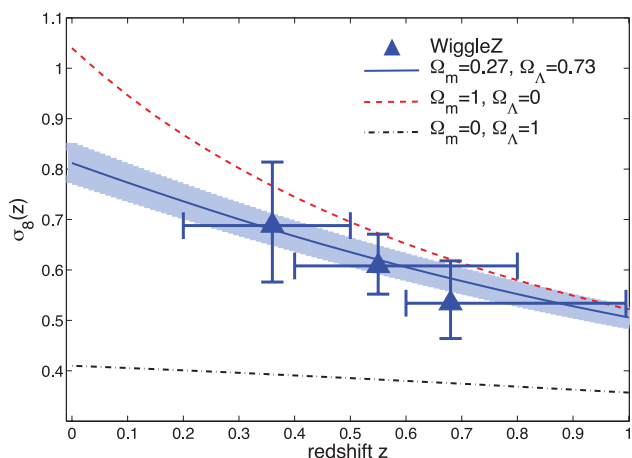

Figure 16. Evolution of $\sigma_8(z)$. The blue symbols correspond to the estimates of $\sigma_8(z_{\mathrm{eff}})$ from the 2PCF and 3PCF of WiggleZ galaxies at different redshifts, marginalizing over the linear and non-linear bias parameters. The blue solid line corresponds to the evolution of $\sigma_8(z)$ in a flat *WMAP*5-ΛCDM universe, with $\Omega_m = 0.27$ and $\sigma_8(z = 0) = 0.812$; the blue shaded region corresponds to combined *WMAP*5 errors. The red dashed line corresponds to the evolution of $\sigma_8(z)$ in a flat $\Omega_m = 1$ CDM universe. The black dash–dotted line shows the evolution of a flat $\Omega_\Lambda = 1$ universe. All models are normalized at the epoch of recombination.

We also plot in Fig. 16 the evolution of σ_8 in two different models of flat universes, an Einstein–de Sitter model (flat $\Omega_m = 1$) and another one with no matter content, just cosmological constant. As *WMAP*5 (Komatsu et al. 2009) measured the amplitude of CMB perturbations at the epoch of recombination $z \sim 1100$, we normalize σ_8 at that redshift for the three cosmologies shown here. We find that an Einstein–de Sitter universe is disfavoured ($\Delta\chi^2 = 3.5$ for one-parameter fit) when combining measurements of the three WiggleZ redshift samples, as well as spatially flat models with low matter content ($\Delta\chi^2 = 45.01$ for $\Omega_m = 0.01$).

6 SUMMARY AND CONCLUSIONS

We have measured the redshift-space two- and three-point clustering statistics for the WiggleZ galaxies and obtained constraints on the linear and non-linear galaxy bias and the cosmological parameter σ_8 at three different epochs. Our results can be summarized as follows.

(i) We obtain significant measurements of the WiggleZ 3PCF, recovering its shape dependence on large scales, spanning a wide redshift range for all regions and subregions (in angle and redshift) of the galaxy sample.

(ii) These measurements are in agreement with standard models for the growth of structure driven by gravitational clustering, reflecting the morphology of the clustering large-scale structures, i.e. the 'cosmic web'.

(iii) Using a simple local bias parametrization along with an empirical treatment of redshift-space distortions of the correlation functions, we get constraints on the bias parameters as a function of redshift. Our estimation of the linear bias agrees with evolution of DM haloes $\sim 10^{12}\,h^{-1}$ M$_\odot$.

(iv) For all our redshift samples, we detect a significant non-zero (negative) non-linear bias, also consistent with the models for the non-linear bias evolution of haloes of masses $\sim 10^{12}\,h^{-1}$ M$_\odot$.

(v) We also constrain the evolution of σ_8 with redshift, and by extension, the evolution of the linear growth factor. We find that our measurements are consistent with the predictions of a *WMAP*5 ΛCDM concordance cosmology and with measurements from other methods and observables.

The improvement in the measurements of the higher order correlations in the last 10 years has been dramatic, and it is remarkable that we can now measure the 3PCF using galaxies up to redshift $z \sim 1$. Although the S/N of the WiggleZ 3PCF is weaker than lower redshift measurements from the SDSS main sample (McBride et al. 2011a,b) and SDSS LRG sample (Kulkarni et al. 2007; Marín 2011), we nonetheless have extended the utility of higher order correlations functions to $z \sim 1$, using the WiggleZ survey data. We note that using JK resampling for error estimation probably overestimates the variance on large scales (Marín 2011); our measurements would be improved by the availability of mock galaxy catalogues. At the same time, with improved statistics we need to improve our modelling of redshift-space distortions and small-scale effects in order to extract as much information as possible from the higher order correlations.

Also, improved modelling would help to combine 3PCF measurements with other observables such as clustering and lensing (see Mandelbaum et al. 2012), two-dimensional redshift-space distortions two-point statistics or the passive galaxies method (Tojeiro et al. 2012).

In the near future, with improved measurement techniques and with bigger surveys, we will be able to use these techniques to measure the growth factor accurately and discriminate between ΛCDM model and modified gravity models (Linder & Cahn 2007).

REFERENCES

Adelman-McCarthy J. K. et al., 2006, ApJS, 162, 38
Bardeen J. M., Bond J. R., Kaiser N., Szalay A. S., 1986, ApJ, 304, 15
Barriga J., Gaztañaga E., 2002, MNRAS, 333, 443
Berlind A. A., Weinberg D. H., 2002, ApJ, 575, 587
Bernardeau F., Colombi S., Gaztañaga E., Scoccimarro R., 2002, Phys. Rep., 367, 1
Beutler F. et al., 2011, MNRAS, 416, 3017
Blake C. et al., 2010, MNRAS, 406, 803
Blake C. et al., 2011a, MNRAS, 415, 2892
Blake C. et al., 2011b, MNRAS, 415, 2876
Cole S. et al., 2005, MNRAS, 362, 505
Contreras C. et al., 2013, MNRAS, 430, 924
Cooray A., Sheth R., 2002, Phys. Rep., 372, 1
Drinkwater M. J. et al., 2010, MNRAS, 401, 1429
Eisenstein D. J. et al., 2005, ApJ, 633, 560
Eke V. R., Cole S., Frenk C. S., 1996, MNRAS, 282, 263
Feldman H. A., Kaiser N., Peacock J. A., 1994, ApJ, 426, 23
Fosalba P., Pan J., Szapudi I., 2005, ApJ, 632, 29
Frieman J. A., Gaztanaga E., 1994, ApJ, 425, 392
Fry J. N., Gaztanaga E., 1993, ApJ, 413, 447
Fu L. et al., 2008, A&A, 479, 9
Gardner J. P., Connolly A., McBride C., 2007, in Shaw R. A., Hill F., Bell D. J., eds, ASP Conf. Ser. Vol. 376, Astronomical Data Analysis Software and Systems XVI. Astron. Soc. Pac., San Francisco, p. 69
Gaztañaga E., Scoccimarro R., 2005, MNRAS, 361, 824
Gaztañaga E., Norberg P., Baugh C. M., Croton D. J., 2005, MNRAS, 364, 620
Gaztañaga E., Cabré A., Castander F., Crocce M., Fosalba P., 2009, MNRAS, 399, 801
Gilbank D. G., Gladders M. D., Yee H. K. C., Hsieh B. C., 2011, AJ, 141, 94
Guo H., Li C., Jing Y. P., Boerner G., 2013, ApJ, preprint (arXiv:1303.2609)
Jing Y. P., Borner G., 1997, A&A, 318, 667
Jing Y. P., Börner G., 2004, ApJ, 607, 140
Kaiser N., 1987, MNRAS, 227, 1
Kayo I. et al., 2004, PASJ, 56, 415
Kazin E. A. et al., 2010, ApJ, 710, 1444
Kilbinger M. et al., 2013, MNRAS, 430, 2200
Komatsu E. et al., 2009, ApJS, 180, 330
Kulkarni G. V., Nichol R. C., Sheth R. K., Seo H.-J., Eisenstein D. J., Gray A., 2007, MNRAS, 378, 1196
Lahav O., Suto Y., 2004, Living Rev. Relativ., 7, 8
Landy S. D., Szalay A. S., 1993, ApJ, 412, 64
Li I. H. et al., 2012, ApJ, 747, 91
Lin H. et al., 2012, ApJ, 761, 15
Linder E. V., Cahn R. N., 2007, Astropart. Phys., 28, 481
Mandelbaum R., Slosar A., Baldauf T., Seljak U., Hirata C. M., Nakajima R., Reyes R., Smith R. E., 2012, MNRAS, preprint (arXiv:1207.1120)
Marín F., 2011, ApJ, 737, 97
Marín F. A., Wechsler R. H., Frieman J. A., Nichol R. C., 2008, ApJ, 672, 849
Martin D. C. et al., 2005, ApJ, 619, L1
McBride C. K., Connolly A. J., Gardner J. P., Scranton R., Newman J. A., Scoccimarro R., Zehavi I., Schneider D. P., 2011a, ApJ, 726, 13
McBride C. K., Connolly A. J., Gardner J. P., Scranton R., Scoccimarro R., Berlind A. A., Marín F., Schneider D. P., 2011b, ApJ, 739, 85
Nichol R. C. et al., 2006, MNRAS, 368, 1507
Norberg P. et al., 2001, MNRAS, 328, 64
Norberg P., Gaztañaga E., Baugh C. M., Croton D. J., 2011, MNRAS, 418, 2435
Pan J., Szapudi I., 2005, MNRAS, 362, 1363
Peacock J. A. et al., 2001, Nat, 410, 169
Peebles P. J. E., 1980, The Large-Scale Structure of the Universe. Princeton Univ. Press, Princeton, NJ
Peebles P. J. E., Groth E. J., 1975, ApJ, 196, 1
Percival W. J. et al., 2007, ApJ, 657, 645
Press W. H., Schechter P., 1974, ApJ, 187, 425
Press W. H., Teukolsky S. A., Vetterling W. T., Flannery B. P., 1992, Numerical Recipes in C. Cambridge Univ. Press, Cambridge
Ross A. J., Brunner R. J., Myers A. D., 2006, ApJ, 649, 48
Rozo E. et al., 2010, ApJ, 708, 645
Sánchez A. G. et al., 2012, MNRAS, 425, 415
Scoccimarro R., Couchman H. M. P., Frieman J. A., 1999, ApJ, 517, 531
Scoccimarro R., Sheth R. K., Hui L., Jain B., 2001, ApJ, 546, 20
Sefusatti E., Scoccimarro R., 2005, Phys. Rev. D, 71, 063001
Sharp R. et al., 2006, Proc. SPIE, 6269, 62690G
Sheth R. K., Mo H. J., Tormen G., 2001, MNRAS, 323, 1
Smith R. E. et al., 2003, MNRAS, 341, 1311
Smith R. E., Sheth R. K., Scoccimarro R., 2008, Phys. Rev. D, 78, 023523
Springel V., White S. D. M., Tormen G., Kauffmann G., 2001, MNRAS, 328, 726
Szapudi S., Szalay A. S., 1998, ApJ, 494, L41
Tojeiro R. et al., 2012, MNRAS, 424, 2339
Verde L. et al., 2002, MNRAS, 335, 432
White S. D. M., Frenk C. S., 1991, ApJ, 379, 52
White S. D. M., Rees M. J., 1978, MNRAS, 183, 341
Yang X., Mo H. J., van den Bosch F. C., 2003, MNRAS, 339, 1057
Zehavi I. et al., 2005, ApJ, 630, 1
Zehavi I. et al., 2011, ApJ, 736, 59

APPENDIX A: WIGGLEZ 3PCF MEASUREMENTS OF ISOSCELES AND VERY ELONGATED TRIANGLES

In Fig. A1, we plot the results of the WiggleZ correlation functions measured for isosceles configurations, where $u = s_2/s_1 = 1$, for the three redshift slices we studied. In these configurations, the third side length runs from $s_3 \sim 0$ on very small angles $\theta \sim 0$, where the bias model we use is no longer valid due to high non-linearities. Since the third triangle side s_3 covers a large range of scales, for purposes of plotting we show the absolute values of the 2PCF and connected 3PCF on a logarithmic scale, while $Q(\theta)$ is shown on a linear scale (which can take positive or negative values). We can observe first that in general the errors in these measurements are smaller compared with the ones we showed in Fig. 5 for the $u = 2$ configurations. As in the $u = 2$ configurations, there is no significant
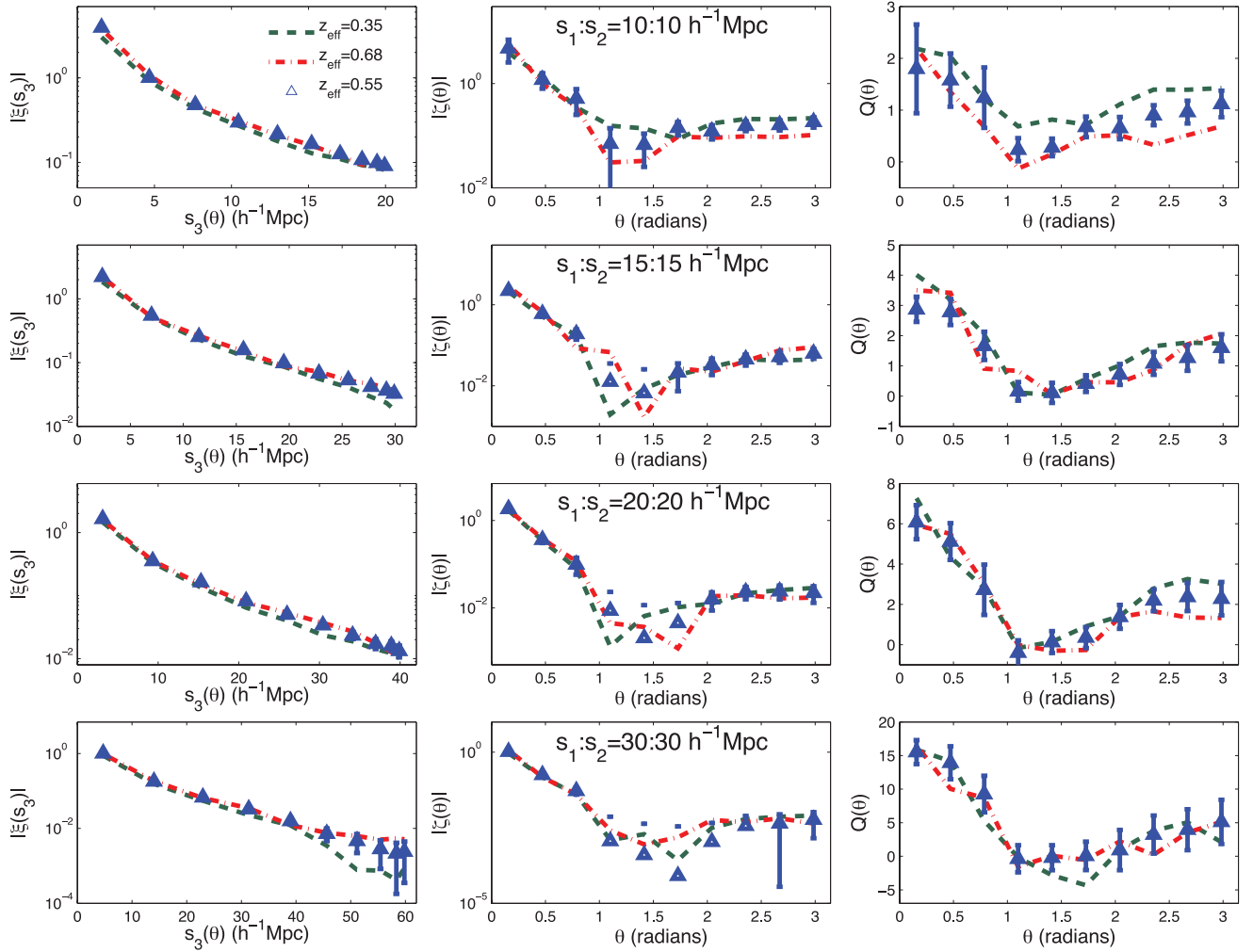
Figure A1. The WiggleZ combined correlations of isosceles triangles ($u = 1$) in redshift space. We show the absolute 2PCF $|\xi(s_3(\theta))|$ (left), absolute connected 3PCF $|\zeta(s, u = 1, \theta)|$ (middle) and reduced 3PCF $Q(s, u = 1, \theta)$ (right) of WiggleZ galaxies in the $z_{eff} = 0.55$ slice (blue triangles), in the slice at $z_{eff} = 0.35$ (green dashed line) and in the $z_{eff} = 0.68$ slice (red dash–dotted line). Errors have been determined by JK resampling.

evolution in the amplitude of the correlation values. The 3PCF of equilateral triangles ($u = 1$, $\theta \sim 1$) is small and even negative, as expected when galaxies cluster in filamentary structures on the largest scales.

In Fig. A2, we plot the results of the WiggleZ correlation functions measured on very elongated configurations, where $u = 3$, for the three redshift slices we studied. For these configurations, the S/N is much smaller than in other u configurations, specially on

large θ. For the $z_{eff} = 0.35$ slice (green dashed line), ζ and Q are poorly measured on the largest scales, justifying our decision to use a maximum separation $s_{3, max}$ smaller than that adopted for the other two redshift slices. Note that we reach scales where the BAO features could in principle be observed $s_3 \sim 100\,h^{-1}$ Mpc, but the WiggleZ low galaxy bias makes it difficult to achieve a significant detection that could be used to constrain cosmological parameters [as claimed by Gaztanaga et al. (2008) for SDSS LRGs].
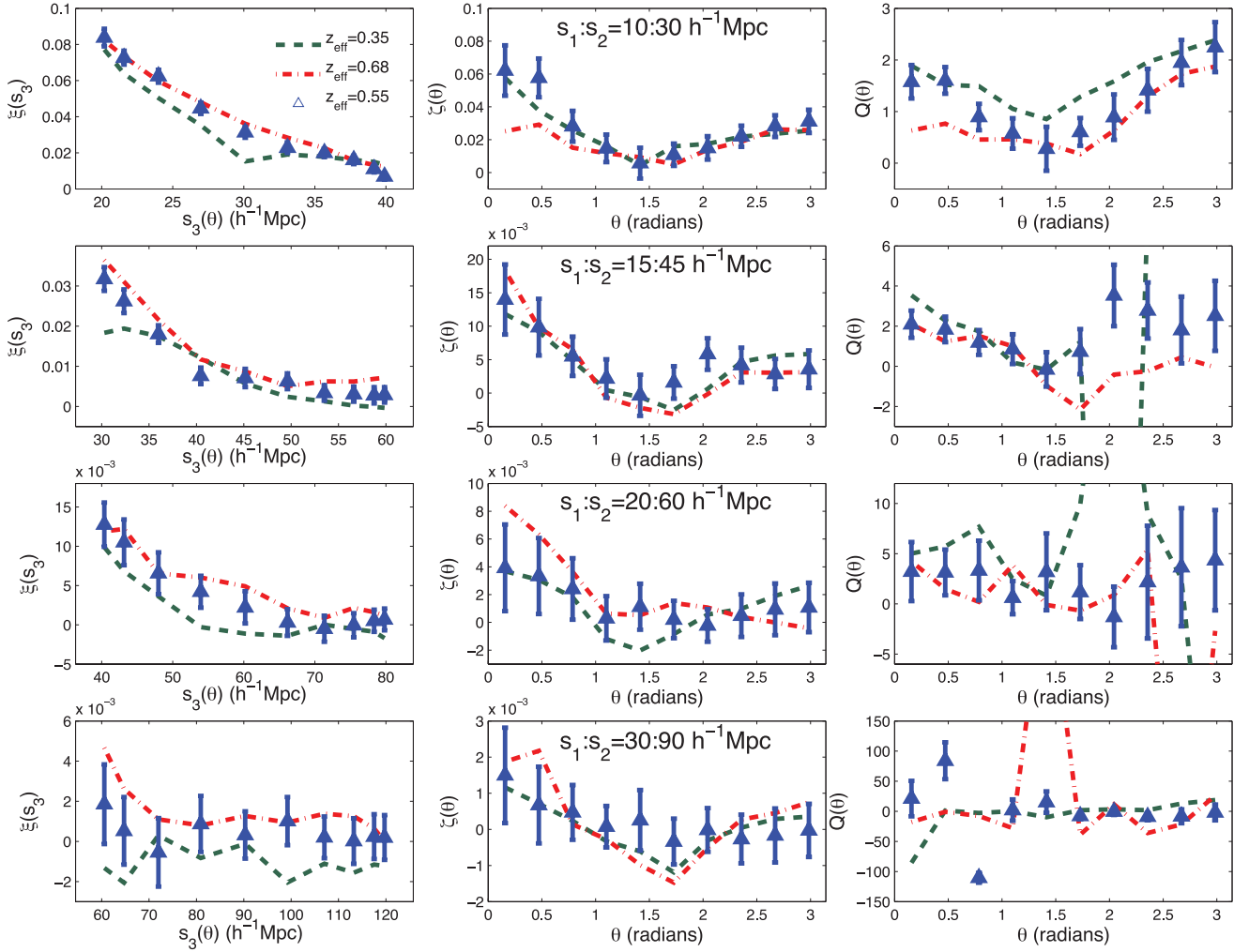
Figure A2. The WiggleZ combined correlations of very elongated triangles ($u = 3$) in redshift space, for the 2PCF $\xi(s_3(\theta))$ (left), connected 3PCF $\zeta(s, u = 3, \theta)$ (middle) and reduced 3PCF $Q(s, u = 3, \theta)$ (right) of WiggleZ galaxies in the $z_{\mathrm{eff}} = 0.55$ slice (blue triangles), in the slice at $z_{\mathrm{eff}} = 0.35$ (green dashed line) and in the $z_{\mathrm{eff}} = 0.68$ slice (red dash–dotted line). Errors have been determined by JK resampling.

This paper has been typeset from a TEX/LATEX file prepared by the author.